Non-Newtonian effects on immiscible viscous fingering in a radial Hele-Shaw cell

John E. Sader, Derek Y. C. Chan, and Barry D. Hughes
Department of Mathematics, University of Melbourne, Parkville, 3052 Victoria, Australia
(Received 7 September 1993)

The displacement of a high-viscosity non-Newtonian fluid by a low-viscosity Newtonian fluid in a Hele-Shaw cell is capable of producing ramified viscous-fingering patterns exhibiting fractal characteristics. Recently, it was established that interfacial tension has little influence on the formation of these fractal patterns. However, the precise mechanism behind their formation is not as yet fully understood. In this paper, we consider the immiscible displacement of a non-Newtonian fluid in a radial Hele-Shaw cell, and present a detailed analysis of the flow, thus exposing features which until now have not been reported. In particular, we find an effective length compression for the formation of viscous-fingering patterns and accelerated growth rates, which upon consideration of recent experimental results, are consistent with the formation of fractal viscous-fingering patterns.

PACS number(s): 47.20.Gv, 47.50.+d, 68.10.−m, 47.53.+n

I. INTRODUCTION

It is well known that the displacement of a high-viscosity non-Newtonian fluid by a low-viscosity Newtonian fluid in a Hele-Shaw cell is capable of producing aborescent viscous-fingering patterns exhibiting fractal characteristics [1–15]. Numerous experimental studies have been conducted to date on the displacement, in an attempt to quantify the effects of different material and geometrical properties on the flow [1–15]. One particularly important observation was made by Van Damme *et al.* [12], where they established that interfacial tension does not inhibit the formation of fractal patterns but only sets a length scale below which the patterns are not fractal. This work therefore settled the point of contention regarding the role of interfacial tension in the development of fractal viscous-fingering patterns.

However, the theoretical investigation of this flow phenomenon for non-Newtonian fluids has been relatively unexplored [5,8,14,16–18]. This is in contrast to the classical displacement of a Newtonian fluid in a Hele-Shaw cell, which has received both extensive theoretical and experimental investigation [3,19–39]. In general, the flow of non-Newtonian fluids in Hele-Shaw cells has been analyzed upon consideration of analogous physical process [1,5,8,14], such as diffusion-limited aggregation, due to the similarity of the resulting viscous-fingering patterns and in some cases the governing equations. However, apart from the work of Pascal [17] and Wilson [18] very little activity has focused on a hydrodynamic analysis of the flow to explain the phenomenon observed. In this paper we investigate the immiscible displacement of a non-Newtonian fluid in a radial Hele-Shaw cell, since it has already been established that interfacial tension does not inhibit the formation of fractal viscous-fingering patterns [12]. We perform a linear stability analysis on the hydrodynamic equations to quantify the influence of non-Newtonian behavior on the formation of fractal viscous-fingering patterns. In doing so, we discover features and properties of the flow arising from the non-Newtonian behavior of the fluid that clearly favor the formation of fractal viscous-fingering patterns.

We note that the non-Newtonian nature of a fluid can be quantified in terms of its elastic and viscous properties. Recently, Wilson [18] performed a similar linear stability analysis for the flow of a purely elastic and purely shear thinning non-Newtonian fluid in a *rectilinear* Hele-Shaw cell. From this analysis, he concluded that the fractal nature of such viscous-fingering patterns is predominantly caused by the effects of elasticity and zero interfacial tension, with shear thinning not displaying any interesting effects. As we shall discuss, Wilson [18] considered a case which does not appear frequently in practice and furthermore some of his conclusions appear to be inconsistent with recent experimental findings.

Our analysis differs from that presented by Wilson [18] in that we analyze the *radial* Hele-Shaw flow problem, which exhibits features not present in the rectilinear flow. For instance, in the radial case there exists a minimum radius below which no perturbations to the expanding interface can grow [23]. Furthermore, as the radius of the interface increases with increasing time, the cutoff wave number above which no perturbations can grow also increases [23]. Thus, in the radial case we are able to examine not only the relative change in the growth rates of the individual perturbations due to the non-Newtonian behavior of the fluid, but also the relative change in the position of the fluid interface at which these perturbations are able to grow. These features of the radial flow geometry will be of fundamental importance in our ensuing discussions on the influence of non-Newtonian behavior on the viscous-fingering patterns.

Pascal [17] recently considered the radial displacement of a shear thinning (power-law) fluid by a different shear thinning (power-law) fluid in porous media. However, he neglected capillary or surface tension effects, i.e., he assumed surface tension to be zero. Since the inclusion of surface tension is of fundamental importance to the analysis of the immiscible displacement of a non-Newtonian fluid in Hele-Shaw cell, the work of Pascal

does not preempt our discussion, as the results we are to present cannot be inferred from those of Pascal [17].

We shall commence by discussing some general physical considerations of the displacement experiments in radial Hele-Shaw cells, which will provide the rationale for the present theoretical model. This will be followed in Sec. III by the main theoretical results of the analysis, with all detailed derivations relegated to the Appendix. Finally a detailed analysis and discussion of these results in light of previous experimental and theoretical findings will be presented in Sec. IV.

II. PRELIMINARY DISCUSSION

In general, non-Newtonian fluids exhibit the effects both of shear thinning and of elasticity. However, examples do occur for which one such effect has been effectively removed, e.g., Boger fluids [11], which are considered to be purely elastic. Furthermore, the flow of non-Newtonian fluids in Hele-Shaw cells is also influenced by other factors, and thus care must be taken in characterizing these fluids. For instance, if the flow is slow enough that the Deborah number De (defined to be the ratio of the elastic relaxation time t_R to the fluid flow time t_{fl}) is far less than unity, then the elastic properties of these fluids will not be exhibited. This appears to be the case in the radial Hele-Shaw displacement experiments of Allen and Boger [11] in which purely elastic Boger fluids were displaced by a low-viscosity driving fluid. Boger fluids have a very high viscosity and an elastic relaxation time in the range $0.5 \lesssim t_R \lesssim 2$ s [40]. Furthermore, the very high viscosity and nonshear thinning nature of these fluids limits the practical rate at which they can be displaced in a Hele-Shaw cell. The result is that the fluid flow time is large, i.e., $t_{fl} \gg 1$ s (the duration of the experiments were of the order of many hours) [41] and hence, in these experimental situations we have $\mathrm{De} \ll 1$. This provides an explanation for the observations of Allen and Boger [11] where the observed fingering patterns for the elastic Boger fluids were similar to those for Newtonian fluids of the same shear viscosity, because the displacement was carried out at a low Deborah number. Hence, the experiments of Allen and Boger [11] on elastic fluids were effectively experiments on Newtonian fluids.

It is clear from the above discussion that if a general viscoelastic fluid were placed in a Hele-Shaw cell and displaced at a rate which gave a very small Deborah number, then the elastic nature of these fluids would not be exhibited, and the fluids would in effect behave as purely shear thinning fluids. This is, of course, provided that the flow was not so slow that the effects of shear thinning would also disappear. Since the characteristic relaxation time t_R of general practical non-Newtonian fluids used in Hele-Shaw experiments, such as [5–8,11], is at most of the order of seconds [40], and the time scale of the displacement in most Hele-Shaw experiments greatly exceeds this, as discussed above, it is clear that Hele-Shaw experiments usually correspond to a regime where $\mathrm{De} \ll 1$. This leaves only the effects of shear thinning to be considered.

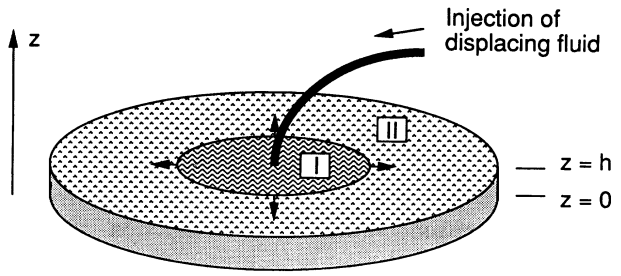

FIG. 1. Schematic illustration of the radial Hele-Shaw cell, showing injection of displacing fluid into region I and the consequent displacement of the fluid in region II. Arrows around the interface between regions I and II indicate the direction of flow. The origin of the cylindrical coordinate system is taken at the center of the bottom plate, with the z direction as indicated.

We should note that elastic effects can be exhibited in flow in Hele-Shaw cells if elastic fluids are used which also exhibit significant shear thinning, since this allows an increase in the injection rate of the displacing fluid, and hence gives a possible increase in the Deborah number. It has been found in experiments using high-volume-fraction colloidal fluids [12,13,42–44] that flows in the high-Deborah-number regime can lead to very interesting effects, although it is unclear whether the patterns observed in these investigations which exhibit fracturelike characteristics are due to the elastic nature of the fluids or the interaction of the colloidal particles. We shall not elaborate on this point any further, since it is beyond the scope of the present paper.

The above discussion gives the motivation behind the choice of a purely shear thinning constitutive equation, to be used in the ensuing analysis. In this paper, we present a linear stability analysis of the immiscible displacement of a purely shear thinning fluid in a radial Hele-Shaw cell (see Fig. 1), and we choose the Ostwald–de Waele power-law model [18,45] to describe the shear thinning property of the non-Newtonian fluid. To simplify the problem, we shall consider an inviscid displacing fluid, such as air, so that we work in the limit of an infinite viscosity ratio, where the viscosity ratio is defined to be the ratio of the displaced fluid viscosity to that of the displacing fluid. We note that the non-Newtonian fluid model considered is also able to display the effects of shear thickening, although this case is less likely to be encountered in practice.

III. MAIN RESULTS

In this section we present the main results from a linear stability analysis which we believe to be of fundamental importance to the understanding of the immiscible displacement of a non-Newtonian shear thinning fluid, the power-law model, by an inviscid fluid in a radial Hele-Shaw cell. For a complete derivation the reader is referred to the Appendix.

We now summarize some notational conventions implemented throughout this paper.

(a) The superscripts (0) and (1), respectively, refer to solutions of the steady-flow problem and perturbation

correction due to fingering.

(b) We use the cylindrical coordinate system (r,θ,z), hence the subscripts r, θ, and z, respectively, refer to the r, θ, and z components of a vector. A similar standard convention will apply to second-order tensors.

(c) With h the distance between the plates, fluid is confined to the region $0<z<h$ (see Fig. 1), and $\bar{X}$ denotes the depth-averaged value of the function X, i.e., $\bar{X}(r,\theta)=h^{-1}\int_0^h X(r,\theta,z)dz$.

We will show present the main results of the linear stability analysis of the non-Newtonian fluid model under consideration, the Ostwald–de Waele power-law model whose constitutive equation is

$$\tau=2m(2\mathbf{e}:\mathbf{e})^{(n-1)/2}\mathbf{e} , \tag{1}$$

where τ is the extra-stress tensor, m is a constant, n is the power-law index with $0<n<2$, and $\mathbf{e}$ is the rate-of-strain tensor. Note that a Newtonian fluid corresponds to $n=1$, whereas a shear thinning fluid has $n<1$, and a shear thickening fluid has $n>1$.

The fluid is assumed to be incompressible so that the continuity equation for the velocity field $\mathbf{u}$ takes the form

$$\nabla\cdot\mathbf{u}=0 . \tag{2a}$$

Inertia and body force effects are neglected from the momentum equation, so that

$$\nabla\cdot\tau=\nabla P , \tag{2b}$$

where P is the pressure.

Throughout the analysis, it is assumed that the streamlines are parallel to the plates. We first consider the flow of the steadily expanding circular front. This will form the base solution on which perturbations will later be imposed. The solution to Eqs. (1)–(2b), corresponding to a constant volumetric injection rate of displacing fluid, is obtained with the imposition of the usual no-slip boundary conditions at the plates

$$P^{(0)}=\begin{cases} G\ln\left[\dfrac{r}{\hat{r}}\right], & n=1 \\ \dfrac{G}{1-n}\left[\dfrac{1}{r^{n-1}}-\dfrac{1}{\hat{r}^{n-1}}\right], & \text{otherwise} , \end{cases} \tag{3a}$$

$$u_r^{(0)}=\frac{1}{r}\left\{-\frac{G}{m}\right\}^{1/n}\frac{n}{1+n}\times\left\{\left[\frac{h}{2}\right]^{(n+1)/n}-\left|z-\frac{h}{2}\right|^{(n+1)/n}\right\} . \tag{3b}$$

Here G is a negative constant, r is the radial coordinate, and h is the plate spacing (see Fig. 1). The radius $\hat{r}(t)$ of the interface at time t is given by

$$\hat{r}(t)=bt^{1/2} \tag{4a}$$

with

$$b=\{2V\hat{r}\}^{1/2}=\left\{\frac{Q_0}{\pi h}\right\}^{1/2} , \tag{4b}$$

where Q_0 is the volumetric flow rate of displacing fluid being injected. We denote the depth-averaged velocity at the interface $u_r^{(0)}|_{r=\hat{r}}$ by V.

We now examine the effects of perturbations to the circular expanding interface, and represent the perturbed interface by

$$r=\hat{r}(t)+\zeta(\theta,t) , \tag{5}$$

where the perturbation $\zeta(\theta,t)$ is assumed to be small, i.e., $|\zeta|\ll\hat{r}$. We consider perturbations of the form

$$\zeta(\theta,t)=f_k(t)\cos k\theta , \tag{6}$$

where the amplitude function $f_k(t)$ is to be determined and k is an integer henceforth referred to as the wave number. To determine the amplitude function $f_k(t)$ we apply a first-order perturbation method to the governing and constitutive equations and upon consideration of the pressure interface condition which takes into account the surface tension γ at the interface, we obtain

$$\frac{1}{f_k}\frac{df_k}{dt}=\frac{G}{P_1\hat{r}^2}\left\{\frac{c(k)}{k^2}-1\right\}-\frac{\gamma(k^2-1)\hat{r}^{n-4}}{P_1} , \tag{7a}$$

where

$$P_1=-\frac{c(k)}{k^2}\frac{G}{\hat{r}V} , \tag{7b}$$

$$c(k)=\frac{1-n+\sqrt{(1-n)^2+4k^2n}}{2} . \tag{7c}$$

The solution of Eq. (7a) gives the amplitude function

$$f_k(t)=At^{1/2\{[k^2/c(k)]-1\}}\times\exp\left\{\frac{2\gamma(k^2-1)}{(2-n)b^{4-n}P_1t^{(2-n)/2}}\right\} , \tag{8}$$

where A is an arbitrary constant.

Clearly, the perturbation will grow only if $(1/f_k)(df_k/dt)>0$. It is clear from Eq. (7a) that there exists a critical radius r_k, such that for $\hat{r}>r_k$ the perturbation characterized by the amplitude function $f_k(t)$, with k being the wave number, is able to grow. Furthermore, this critical radius is obtained from Eq. (7a) by setting $(1/f_k)(df_k/dt)=0$ and solving for $\hat{r}$. We must emphasize that the critical radius r_k is, of course, dependent on k.

With the amplitude function $f_k(t)$ given by Eq. (8), we can examine the effects of shear thinning or shear thickening on the growth of perturbations. However, in order to make sensible comparisons, it is essential to establish a common length scale. We shall use the length scale associated with the Newtonian fluid ($n=1$), which is a natural choice. The scaling is achieved by setting the critical radius r_{k_0}, at which the lowest wave number $k=k_0$ is able to grow, to be identical to the Newtonian value, for all values of n. Since $(1/f_k)(df_k/dt)=0$ for $k_0=1$ always, it is clear from Eq. (7a) that the minimum value for k_0 is $k_0=2$. For flow in general radial Hele-Shaw experiments, the lowest wave number k_0 that is able to grow is $k_0=2$. However, with the imposition of geometrical re-

strictions in the Hele-Shaw cell, such as induced anisotropy, this value of k_0 may change, as will be seen in the next section. From the above discussion, we immediately see that the appropriate scaling length "a" for the radial coordinate r is identical to the Newtonian result [28,30]

$$r \sim a = \frac{\pi \gamma h^3}{Q_0 \eta} , \tag{9}$$

where η is the Newtonian viscosity and is related to m in Eq. (1) by

$$m = \frac{3(k_0-1)}{k_0^2 - c(k_0)} \left[\frac{k_0+1}{6} \right]^{n-1} \times \left[\frac{k_0 n}{2n+1} \right]^n \left[\frac{\pi^2 \gamma h^5}{Q_0^2} \right]^{n-1} \eta^{2-n} . \tag{10}$$

Note that Eq. (9) differs from the Newtonian result presented in [30] by a factor of π, because we have chosen the starting normalized radius of the minimum possible wave number $k_0=2$, to be unity instead of π as in [30]. The relations presented in Eqs. (9) and (10) enable us to compare the displacement of a Newtonian fluid of viscosity η to that of a power-law fluid, with both fluids being displaced by air in a radial Hele-Shaw cell.

Therefore, using Eq. (9) we are able to normalize the results presented in Eqs. (2)–(8), from which we obtain the following important results. For the remainder of this paper, R refers to the scaled radial coordinate, i.e., $R = r/a$ with "a" as defined in Eq. (9). The normalized critical radius R_k is then obtained from Eq. (7a), as discussed above,

$$R_k = \left\{ \frac{k^2 - c(k)}{k_0^2 - c(k_0)} \frac{k_0^2 - 1}{k^2 - 1} \frac{k_0^n}{k^2} \left[\frac{k_0+1}{6} \right]^{n-2} \right\}^{1/(n-2)} . \tag{11}$$

Setting $k=k_0$, we recover the Newtonian normalized critical radius $R_k^{(N)}$,

$$R_k^{(N)} = \frac{k_0(k_0+1)}{6} , \tag{12}$$

as required.

The amplitude function $f_k(t)$ can be expressed in terms of the mean normalized interface radius $\hat{R}$ (related to $\hat{r}$ by $\hat{R} = \hat{r}/a$) using Eqs. (4a) and (9),

$$f_k(\hat{R}) = B \hat{R}^{\alpha} \exp \left\{ \frac{\alpha}{2-n} \left[\frac{\hat{R}}{R_k} \right]^{n-2} \right\} , \tag{13}$$

where B is an arbitrary constant, and

$$\alpha = \frac{k^2}{c(k)} - 1 . \tag{14}$$

In the following section we shall examine the implications of these results.

IV. DISCUSSION

A. General discussion of results

In the present section we shall mainly discuss results displaying the effects of shear thinning behavior, as this is the case of general practical interest. However, for completeness we shall also briefly discuss the effects of shear thickening since this feature is naturally incorporated in the present fluid model.

We begin by examining the dependence of the normalized critical radius R_k on the power-law index n for perturbations with different wave numbers k. In particular, we shall consider the case of $k_0=2$ since this is the minimum allowable value for k_0. Plots of R_k vs n for different wave numbers k are presented in Figs. 2(a)–2(d), from which it is clear that a reduction in the power-law index n produces a corresponding decrease in the normalized critical radius R_k. As a numerical example, we compare the behavior of the power-law model (with $n=0.2$) to the Newtonian model ($n=1$). From Figs. 2(a) and 2(b), it is clear that at a normalized mean radius of $\hat{R}=5$ the highest wave number which is able to grow is $k=5$ for the Newtonian case whereas for the power-law model (with $n=0.2$) it is $k=9$, thus demonstrating that a reduction in n, which corresponds to shear thinning, produces a large reduction in R_k for a given wave number. Note that R_k for $k=k_0=2$ is constant for all n, due to the manner in which we have chosen to compare the power-law fluid to the Newtonian fluid, i.e., by using Eqs. (9) and (10), and implementing the same scaling length in all cases. It must also be noted that similar effects on R_k were obtained for other choices of k_0.

We now examine the effects of the power-law index n on the growth rates of the perturbations, as characterized by the amplitude function f_k. It must be noted that instead of presenting f_k as a function of time t, it will be presented as a function of the mean interface radius $\hat{r}$ or, more precisely, as a function of the normalized mean interface radius $\hat{R}$. From Eqs. (4a) and (9) and taking the scaling for time t to be $t \sim a/\overline{u_r^{(0)}}|_{r=a}$, it can be easily shown that $\hat{R}^2 = 2T$, where T is the normalized time. In Figs. 3(a)–3(d), plots are given of $f_k(\hat{R})/\hat{R}$ vs $\hat{R}$ for different values of n and k, with $k_0=2$. Note that the normalization of $f_k(\hat{R})$ is purely arbitrary and we have chosen to present results with $f_k(R_k)/R_k = 1$, for all values of k. Furthermore, we present results only for $\hat{R} > R_k$, because this is the regime in which the perturbations can grow. As is clear from Figs. 3(a)–3(d), decreasing the power-law index n dramatically increases the growth rate of individual perturbations. The dramatic increase in growth rates with decreasing power-law index n, is more evident if one notes the very different range of the abscissa in Figs. 3(a)–3(d).

To examine the overall effect of the above-mentioned properties, we shall produce viscous-fingering patterns of the fluid interface and monitor the effect of varying the fluid characteristics and other properties such as anisotropy induced in the Hele-Shaw cell, on their evolution in time. We can produce these viscous-fingering patterns in

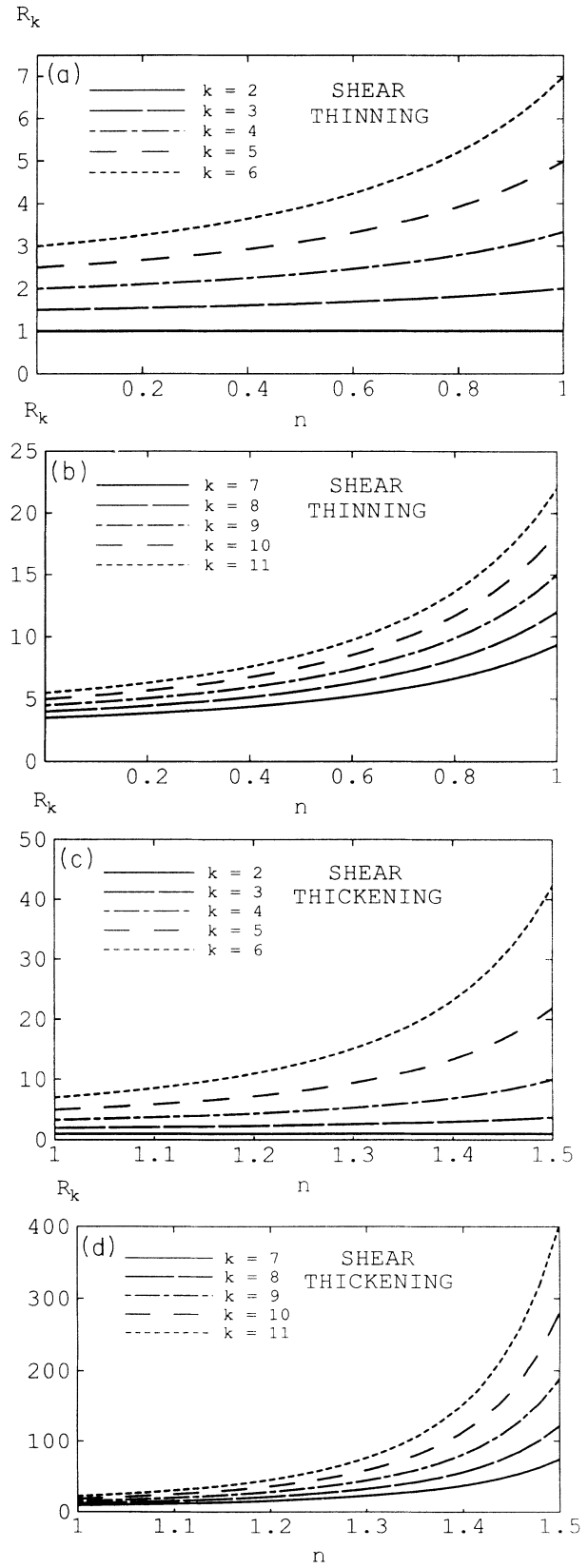

FIG. 2. The normalized critical radius R_k as a function of the power-law index n for various values of wave number k. (a) Shear thinning results ($n \leq 1$) for $k = 2,3,\ldots,6$; (b) shear thinning results ($n \leq 1$) for $k = 7,8,\ldots,11$; (c) shear thickening results ($n \geq 1$) for $k = 2,3,\ldots,6$; (d) shear thickening results ($n \geq 1$) for $k = 7,8,\ldots,11$.

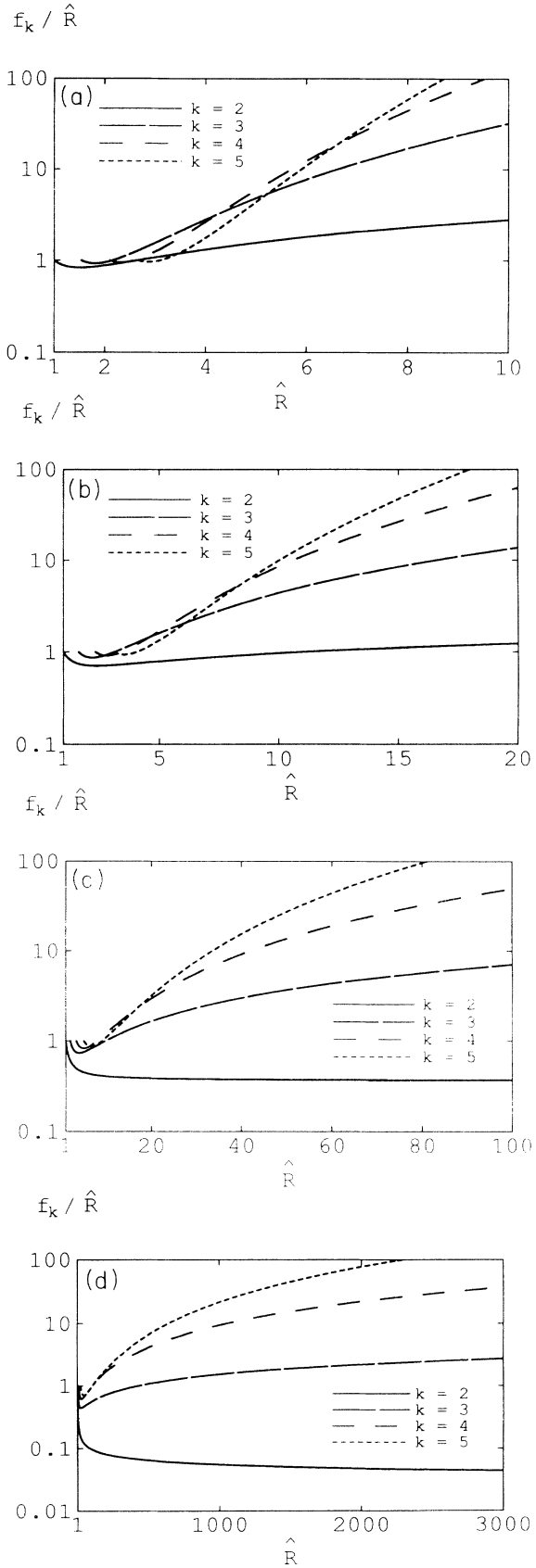

FIG. 3. Amplitude function f_k over normalized mean radius $\hat{R}$, i.e., $f_k/\hat{R}$ as a function of $\hat{R}$ for $k = 2,3,4,5$. (a) Shear thinning results ($n = 0.2$); (b) shear thinning results ($n = 0.5$); (c) Newtonian results ($n = 1$); (d) shear thickening results ($n = 1.5$).

the following manner. We begin with an initially circular interface which is steadily expanding under a constant volumetric injection rate of displacing fluid. When its normalized radius $\hat{R}$ reaches the smallest critical radius R_{k_0} of which the perturbation with the smallest wave number k_0 can grow, a perturbation with this wave number is initiated on the circular interface with a certain magnitude and phase. The interface then continues to expand, together with the imposed perturbation, until its normalized mean radius $\hat{R}$ reaches the next smallest normalized critical radius R_k for which a second perturbation with wave number k can begin to grow. A second perturbation to the interface with this wave number is then initiated with a certain magnitude and phase. This process continues, with the interface accumulating more perturbations as it expands, thus producing a growing viscous-fingering pattern. We emphasize that we have only carried out a linear stability analysis which tracks the development of small-amplitude perturbations ($|f_k| \ll \hat{r}$) about an initially circular interface. It is clear from the above discussion, that apart from the first perturbation, all subsequent perturbations are added to an interface which is noncircular. However, if the noncircularity of the interface is small than it is reasonable to expect an accurate result for f_k of the second and subsequent perturbations, derived under the assumption of an initially circular interface. Therefore, there exists a time period in the initial growth of fingers where a linear stability analysis is valid. To quantify this and demonstrate the above-mentioned properties, we present in Fig. 4 the root-mean-square value of the sum of all perturbations obtained from the linear stability analysis which are able to grow, normalized by $\hat{R}$, henceforth denoted $[\sum_k f_k/\hat{R}]_{\text{rms}}$, for differing values of n. Note that each perturbation in Fig. 4 has been set to have an initial value of $\sqrt{2}$ at its inception, i.e., $f_k(R_k)=\sqrt{2}$, since this conveniently sets $[\sum_k f_k/\hat{R}]_{\text{rms}}$ to be unity at $\hat{R}=1$ and allows a simple linear rescaling of the diagram for different choices of $f_k(R_k)$. The jump discontinuities in Fig. 4 are the result of the introduction of perturbations with increasing wave numbers. The results in Fig. 4 demonstrate that decreasing n decreases the length of the initial growth period for which the linear stability analysis can be used to predict the shape of the fluid interface. This initial growth period is controlled by the noncircularity of the interface and the constraint $|f_k| \ll \hat{r}$, which can be both inferred from $[\sum_k f_k/\hat{R}]_{\text{rms}}$. Furthermore, this decrease in the initial growth period is also accompanied by a reduction in R_k and an increase in growth rates. Thus, we would expect viscous-fingering patterns obtained by a linear stability analysis to be valid in the regime $[\sum_k f_k/\hat{R}]_{\text{rms}} \ll 1$. This region of validity can be found from the results presented in Fig. 4 and proves to be useful in assessing the validity of the following results.

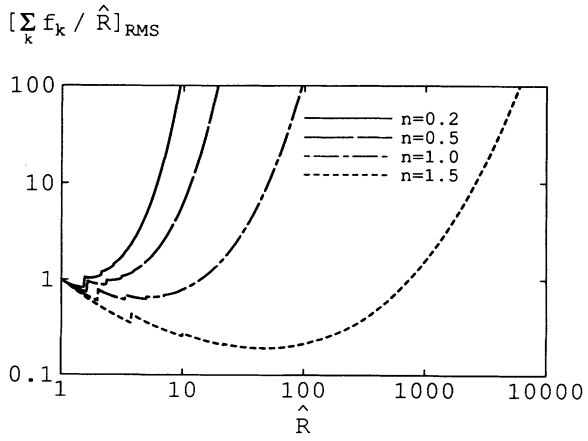

FIG. 4. rms value of sum of all perturbations over the normalized mean radius $\hat{R}$, i.e., $[\sum_k f_k/\hat{R}]_{\text{rms}}$ as a function of $\hat{R}$ for power-law indices of $n=0.2, 0.5, 1, 1.5$.

We can now produce "time lapse" plots of the viscous-fingering patterns. In Figs. 5(a)–5(c) we show such patterns for different values of power-law index n. In order to compare results for different values of n, all perturbations are introduced at an initial magnitude of $f_k=0.01$ and zero phase, and only perturbations involving $\cos 2\theta$, $\cos 3\theta$, $\cos 4\theta$, etc., are considered, corresponding to the onefold symmetry case. It is clear from Figs. 5(a)–5(c), that decreasing n dramatically decreases the time at which a given viscous-fingering pattern is obtained, even though perturbations initially begin to grow at the same time, i.e., for $k=k_0$. As an example, we note that the final patterns presented in Figs. 5(a) and 5(b) are very similar. However, the pattern obtained in Fig. 5(a) corresponding to a power-law fluid (with $n=0.5$) was obtained at a normalized mean interface radius of $\hat{R}=12.9$, whereas the pattern in Fig. 5(b) corresponding to a Newtonian fluid ($n=1$) was obtained for $\hat{R}=57$. This demonstrates that decreasing n provides an effective "length compression" of the growth of viscous-fingering patterns. We found that if we continue to use the results of the linear stability analysis to evolve the fluid interface to large times, certain points on the interface will eventually have a velocity directed towards the injection point. We have used this unphysical result to set the upper bound to the applicability of the linear stability analysis. In all cases presented, we found that the largest viscous-fingering pattern obtained corresponds to a rms value for the sum of all perturbations to be ~ 0.1 of the normalized mean interface radius. This is certainly within the limitations of the linear stability analysis. We can obtain patterns similar to those obtained in Figs. 5(a)–5(c) by using different values for the initial magnitudes of the perturbations. However, increasing the initial magnitude of the perturbations decreases the range of applicability of the analysis, as is clear from Fig. 4, but the patterns clearly grow faster, thus resulting in similar patterns. As we shall see, the value of $f_k=0.01$ for the initial perturbation amplitude was chosen since it gave patterns in good agreement with those obtained experimentally, although this choice is quite arbitrary.

The accelerated growth patterns we obtained are also seen with perturbations possessing other symmetries. In Figs. 6(a)–6(c), we present the growth of the interface for perturbations with fourfold symmetry, i.e., only perturbations involving $\cos 4\theta$, $\cos 8\theta$, $\cos 12\theta$, etc., are included. All perturbations are onset at an initial amplitude of

$f_k = 0.01$ and zero phase. These patterns agree well with the initial patterns obtained experimentally where the same fourfold anisotropy has been introduced to the Hele-Shaw cell by etching the cell walls in two orthogonal directions [29]. Note that we have only shown patterns for which all points on the interface possess a positive velocity away from the injection point, which as discussed above, is the limitation of our analysis.

Finally, we present results of the initial viscous-fingering patterns where no anisotropy has been included. To accomplish this we introduce perturbations of arbitrary magnitude and arbitrary phase. The initial amplitude $f_k(R_k)$ is chosen randomly in the range of 0–0.01, whereas the phase is chosen randomly between 0 and 2π. The interfacial patterns corresponding to such random perturbations are presented in Figs. 7(a)–7(c), for different power-law indices n. Again note the effective length compression and accelerated growth rates in these patterns for decreasing values of n. These patterns are also in excellent agreement with those found in the literature [23,30] for short times after the initial onset of fingering. These patterns were again allowed to grow provided that all points on the interface possessed a positive velocity away from the injection point.

Thus we may summarize the above results as follows:

(a) Shear thinning has the effect of providing a length compression and accelerating growth rates of fingering patterns in comparison to Newtonian fluids, thus leading to viscous-fingering patterns being developed much more rapidly.

(b) In contrast, shear thickening has the opposite effect, thus leading to an effective length "expansion" and viscous-fingering patterns being developed much more slowly relative to Newtonian fluids.

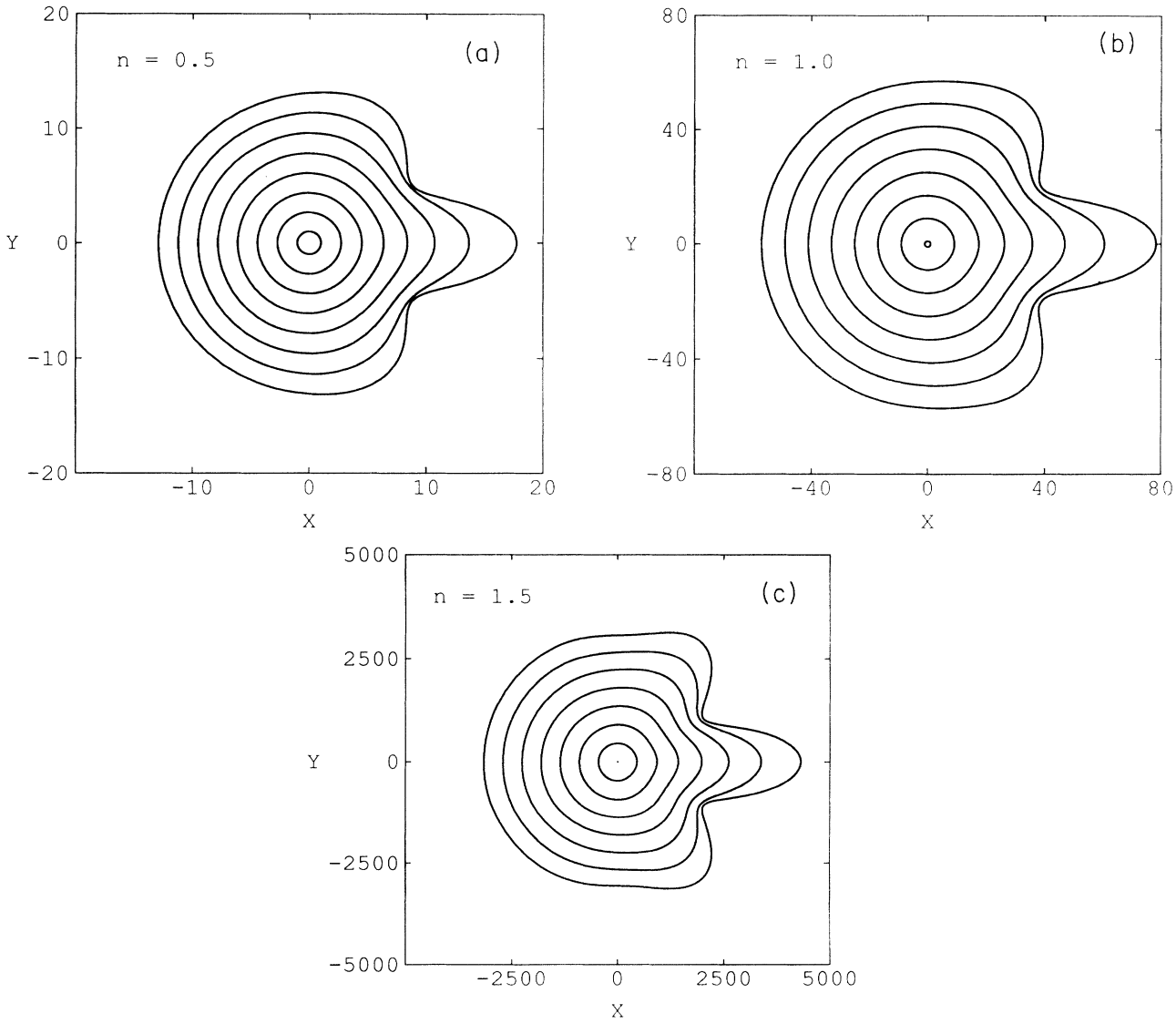

FIG. 5. Growth of interface pattern for a onefold symmetry case with the initial interface at $\hat{R} = 1$. X and Y are the Cartesian components of the normalized cylindrical coordinate system. (a) $n = 0.5$, and interfaces are at intervals of $\hat{R} = 1.7$; (b) $n = 1$, and interfaces are at intervals of $\hat{R} = 8$; (c) $n = 1.5$, and interfaces are at intervals of $\hat{R} = 450$.

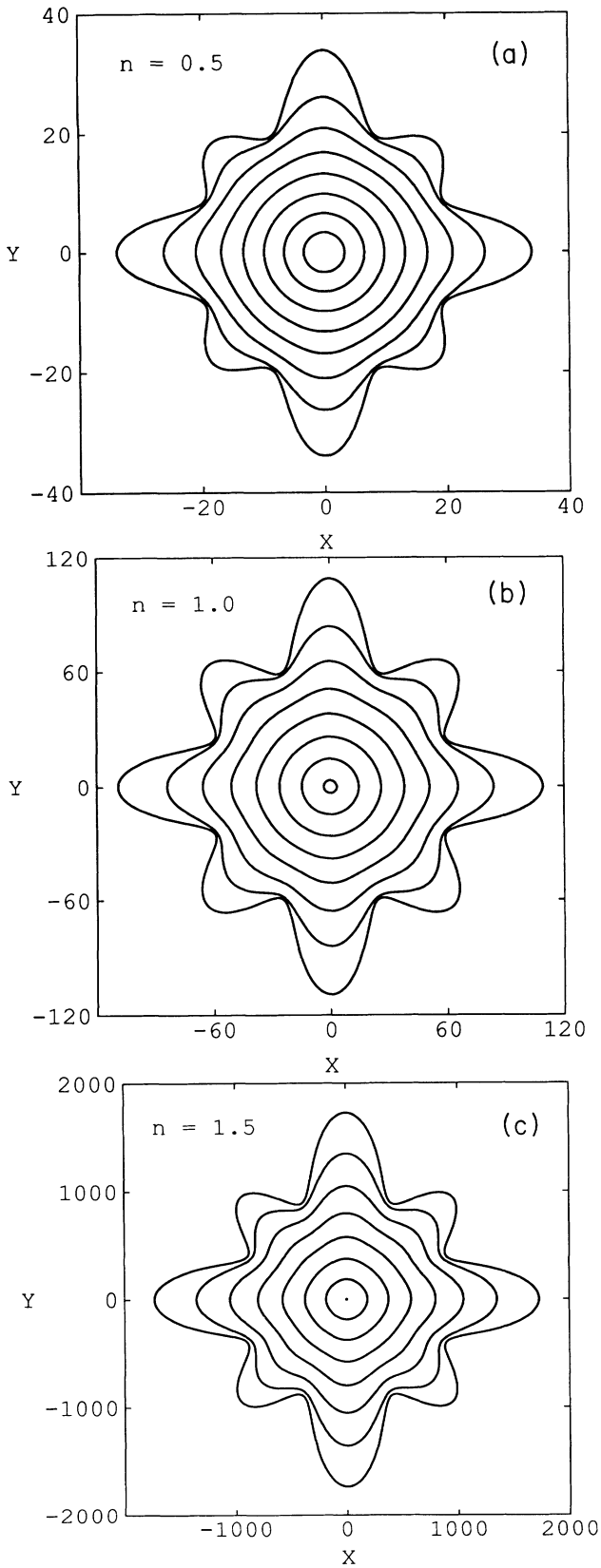

FIG. 6. Growth of interface pattern for a fourfold symmetry case with the initial interface at $\hat{R}=3.333$. X and Y are the Cartesian components of the normalized cylindrical coordinate system. (a) $n=0.5$, and interfaces are at intervals of $\hat{R}=3.2$; (b) $n=1$, and interfaces are at intervals of $\hat{R}=11.2$; (c) $n=1.5$, and interfaces are at intervals of $\hat{R}=180$.

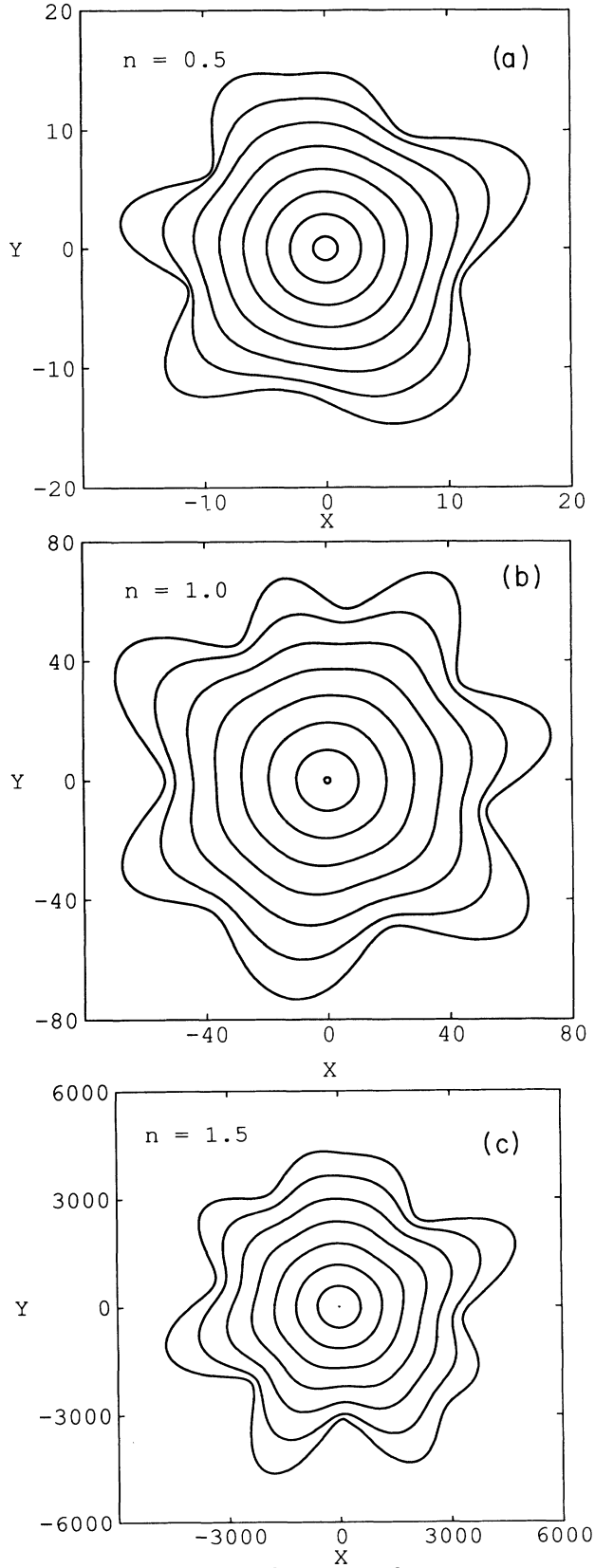

FIG. 7. Growth of interface pattern for zero symmetry case with the initial interface at $\hat{R}=1$. X and Y are the Cartesian components of the normalized cylindrical coordinate system. (a) $n=0.5$, and interfaces are at intervals of $\hat{R}=1.9$; (b) $n=1$, and interfaces are at intervals of $\hat{R}=9.2$; (c) $n=1.5$, and interfaces are at intervals of $\hat{R}=580$.

(c) Initial viscous-fingering patterns can be constructed from the linear stability analysis for reasonably long periods of time, and these show good agreement with experimental results in the literature;

(d) The fingering patterns can also be constructed for different anisotropies introduced into the Hele-Shaw cell.

The physical implications of these results are truly significant in the formation of fractal viscous-fingering patterns, as we shall now discuss in detail.

B. Discussion of fractal pattern formation

It is well known, as we previously stated, that the displacement of a non-Newtonian fluid by a low-viscosity Newtonian fluid in a Hele-Shaw cell is capable of producing aborescent viscous-fingering patterns exhibiting fractal characteristics. The aim of this paper is to establish the mechanism behind this behavior for the immiscible displacement of a purely shear thinning non-Newtonian fluid in a radial Hele-Shaw cell. However, we must emphasize that the results presented in the preceding section were obtained from a linear stability analysis of the flow and therefore fractal patterns at large times are clearly unattainable from the analysis. Nonetheless, a great deal can be learned about the flow and the mechanism involved in the formation of viscous-fingering patterns upon consideration of these results.

It is well known that increasing the tip velocity of the interface, in particular the leading front of a finger, increases the tendency for tip splitting and thus leads to more ramified fingering patterns. It was shown in the preceding section that decreasing the power-law index n dramatically increases the growth rates of the perturbations to the interface and provides an effective length compression for the formation of viscous-fingering patterns, thus enabling viscous-fingering patterns to develop much more rapidly. Thus, decreasing the power-law index n should lead to greater tip splitting and hence more ramified viscous-fingering patterns. As noted above, our results were obtained from a linear stability analysis, and hence effects such as tip splitting clearly cannot be exhibited. However, it is clear from Figs. 2(a)–2(d) that decreasing n also decreases the critical wavelength $\lambda_c \equiv 2\pi R / k_m$ (where k_m is the maximum wave number which allows growth) for a given normalized radius R, which will in turn lead to more ramified patterns. However, these results are not sufficient to conclude that the effects of shear thinning will result in viscous-fingering patterns exhibiting fractal characteristics. We therefore refer to the experimental results of Chen [30] and May and Maher [32], where it was shown experimentally that fractal viscous-fingering patterns form in the immiscible displacement of Newtonian fluids in Hele-Shaw cells when many stages of tip splitting have occurred. We also note the recent work of Jasnow and Yeung [39], who offered numerical evidence that under a constant volumetric injection rate Q_0, radial Hele-Shaw patterns for Newtonian fluids are not asymptotically fractal. However, as they stated [39], this does not preclude the possibility of a range of data which exhibit effective fractal properties. Since we have established that the displacement of a shear thinning fluid will lead to viscous-fingering patterns being developed much more rapidly than the displacement of Newtonian fluids, then with the knowledge of the effects in Newtonian fluids [30,32] and that of tip splitting, we can conclude that the displacement of shear thinning fluids will lead to viscous-fingering patterns exhibiting fractal characteristics being developed at a much earlier stage (or smaller normalized radius) than that of the displacement of Newtonian fluids. In contrast, the displacement of shear thickening fluids should delay the onset of viscous-fingering patterns exhibiting fractal characteristics in comparison to the displacement of Newtonian fluids.

We shall now comment on some previous analyses of the displacement of non-Newtonian fluids in Hele-Shaw cells which are apparently inconsistent with the results we presented and with recent experimental findings.

Recently, Wilson [18] conducted an analysis of the displacement of both purely elastic and purely shear thinning non-Newtonian fluids in a rectilinear Hele-Shaw cell, from which he attributed the formation of fractal viscous-fingering patterns to the effects of elasticity and zero interfacial tension. However, we note that in general experimental situations [1–12], the non-Newtonian fluids involved appear to be predominantly shear thinning, as was discussed by Wilson [18] for the clay pastes in [9,10,42], and this is in line with our discussion of this topic in Sec. II. Wilson [18] actually considered the regime of $\mathrm{De} \gtrsim 1$, i.e., where elastic effects are important in the flow. In contrast, we have considered the general practical regime for flows in radial Hele-Shaw cells where $\mathrm{De} \ll 1$. Thus elasticity need not be considered as it clearly has no effect, as we discussed previously. Also, as was speculated by Nittmann *et al.* [6] and shown experimentally by Van Damme *et al.* [12], interfacial tension does not inhibit the formation of fractal viscous-fingering patterns but simply sets a length scale below which the viscous-fingering patterns are certainly not fractal. This is in contradiction to the conclusion of Wilson [18] who stated that interfacial tension is a predominant factor in the formation of viscous-fingering patterns exhibiting fractal characteristics. Thus, with elasticity and interfacial tension removed as major influences in the formation of fractal viscous-fingering patterns in general practical situations, the only property of a non-Newtonian fluid left to contribute to the formation of fractal fingering patterns is shear thinning. Wilson's conclusion [18] that shear thinning has no significant effect on fractal fingering formation must be treated with care, since it is only valid when $\mathrm{De} \gtrsim 1$ and this is not usually the case of interest for radial Hele-Shaw flows.

Daccord and Nittmann [8] presented a semitheoretical argument which led to the conclusion that the displacement of purely shear thinning fluids does not exhibit increased growth rates in viscous-fingering pattern formation in comparison to Newtonian fluids. They were led to this by first concluding that shear thinning fluids show more tendency for growth on the tips of the fingers than in the bulk, which seems to be valid since it was obtained with only the assumption of streamlines parallel to the plates. However, their calculation of the pressure distri-

bution was obviously obtained for a purely radially symmetric flow, such as is the case in the steadily expanding circular front, which is strictly not applicable when large fingers have already formed. Thus, their conclusion that to first approximation shear thinning does not change the growth rate of viscous-fingering patterns, we feel must be treated with caution.

V. CONCLUSION

Recently, it was established that the immiscible displacement of a high-viscosity non-Newtonian fluid by a low-viscosity Newtonian fluid is capable of producing aborescent viscous-fingering patterns exhibiting fractal characteristics. In this paper, we presented an analysis of the immiscible displacement of a purely shear thinning non-Newtonian fluid in a radial Hele-Shaw cell, in order to quantify the mechanism involved in the formation of these ramified patterns. As a consequence, we found that the displacement of shear thinning fluids has the following properties in comparison to the displacement of Newtonian fluids:

(i) Decreasing the power-law index n enables perturbations to the interface with higher wave numbers to commence growing earlier.

(ii) Decreasing the power-law index n increases the growth rates of individual perturbations to the interface.

(iii) As a consequence of (i) and (ii), viscous-fingering patterns are able to develop much more rapidly, i.e., similar viscous-fingering patterns are able to be produced for the displacement of shear thinning fluids for a lower normalized radius than the displacement of Newtonian fluids.

In contrast, the displacement of shear thickening fluids has the opposite effect, however these fluids are not of great practical significance, as we discussed. Furthermore, upon consideration of recent experimental results on fractal pattern formation using Newtonian fluids and our conclusion (iv), it is clear that the displacement of shear thinning fluids will produce fractal viscous-fingering patterns earlier than Newtonian fluids, whereas shear thickening fluids will in fact delay the onset of fractal pattern formation.

ACKNOWLEDGMENT

This research was supported in part by Australian Research Council Grant No. A69230979.

APPENDIX

In this appendix, we present the formal detailed derivation of the results presented in Sec. III. The relevant coordinate system implemented is as shown in Fig. 1.

The governing equations for the flow are the continuity and momentum equations defined in Eqs. (2a) and (2b), which are to be solved with the imposition of the usual no-slip boundary conditions at the plates, i.e.,

$$\mathbf{u}=\mathbf{0} \quad \text{at } z=0 \text{ and } z=h \ , \tag{A1}$$

for the Ostwald–de Waele power-law model [18], whose constitutive equation is presented in Eq. (1).

Before continuing with the analysis we note that when $n<1$ the power-law model exhibits the characteristics of shear thinning, whereas for $n>1$ it exhibits the characteristics of shear thickening, although as noted earlier the latter case is less likely to be encountered in practice. To proceed with the analysis, we initially consider the steady-flow problem, i.e., the expanding circular front.

Clearly in this case the velocity vector possesses only a radial component u_r which is furthermore radially symmetric, i.e., no angular variation. Then from the continuity equation it is clear that

$$u_r=\frac{u_0(z)}{r} \ , \tag{A2}$$

where $u_0(z)$ is purely a function of z. Furthermore, we emphasize the fundamental restriction for flow in a Hele-Shaw cell [21]:

$$r \gg h \ . \tag{A3}$$

This restriction will be of fundamental importance in the ensuing analysis.

Therefore, from Eqs. (A2) and (A3) it can be easily shown in a similar manner to [45] that Eq. (1) is well approximated by

$$\tau=2m\left|\frac{1}{r}\frac{du_0}{dz}\right|^{n-1}\mathbf{e} \ . \tag{A4}$$

From the fundamental restriction given in Eq. (A3), it is clear that the true length scale "a" for the radial coordinate r is far greater in magnitude than that for the z coordinate which is simply the plate spacing h. However, we need not define a but simply note the property

$$a \gg h \ . \tag{A5}$$

Then, upon substitution of Eq. (A4) into Eq. (2b), it can be easily shown for a constant volumetric injection rate of displacing fluid, that the solution to the steady-flow problem is

$$P^{(0)}=\begin{cases} G\ln\left[\dfrac{r}{\hat{r}}\right], & n=1 \ ; \\ \dfrac{G}{1-n}\left[\dfrac{1}{r^{n-1}}-\dfrac{1}{\hat{r}^{n-1}}\right], & \text{otherwise} \ , \end{cases} \tag{A6a}$$

$$\begin{aligned} u_r^{(0)}&=\frac{u_0(z)}{r} \\ &=\frac{1}{r}\left\{-\frac{G}{m}\right\}^{1/n}\frac{n}{1+n} \\ &\quad\times\left\{\left[\frac{h}{2}\right]^{(n+1)/n}-\left|z-\frac{h}{2}\right|^{(n+1)/n}\right\}, \end{aligned} \tag{A6b}$$

$$\tau_{rr}^{(0)}=-\tau_{\theta\theta}^{(0)}=-\frac{2mu_0}{r^{n+1}}\left|\frac{G}{m}\left[z-\frac{h}{2}\right]\right|^{(n-1)/n} , \tag{A6c}$$

$$\tau_{rz}^{(0)}=-\frac{G}{r^n}\left[\frac{h}{2}-z\right], \tag{A6d}$$

with the extra-stress tensor τ being symmetric and all other components of τ being identically zero. Furthermore, G is a negative constant which is related to the volumetric flow rate of injected fluid, as we shall show shortly, and $\hat{r}$ is the interface radius, which upon consideration of conservation of volume can be easily shown to be related to time t by

$$\hat{r}(t)=bt^{1/2}, \tag{A7a}$$

where

$$b=\{2V\hat{r}\}^{1/2}=\left\{\frac{2n}{2n+1}\left[-\frac{G}{m}\right]^{1/n}\left[\frac{h}{2}\right]^{(n+1)/n}\right\}^{1/2}=\left\{\frac{Q_0}{\pi h}\right\}^{1/2}, \tag{A7b}$$

where V denotes the depth-averaged velocity at the interface $u_r^{(0)}|_{r=\hat{r}}$ and Q_0 is the volumetric flow rate of displacing fluid being injected. Hence Eq. (A7b) gives the relation between Q_0 and G. Note that Eq. (A6a) has been presented with the condition that $P^{(0)}=0$ at the interface, since changing the pressure by an additive constant has no effect on the flow.

With all results for the steady-flow problem thus collected, we turn our attention to the investigation of the effects of perturbations to the steadily expanding circular interface. We therefore introduce a perturbation $\zeta(\theta,t)$ to the initially circular interface. Hence, the equation for the interface becomes

$$r=\hat{r}(t)+\zeta(\theta,t), \tag{A8a}$$

where

$$\zeta(\theta,t)=f_k(t)\cos k\theta, \tag{A8b}$$

with the amplitude function $f_k(t)$ to be determined; k is an integer also referred to as the wavenumber. Furthermore, it is assumed that $|\zeta|\ll\hat{r}$.

Then by performing a first-order perturbation analysis on the constitutive equation Eq. (A3a), it can be shown in a straightforward manner, upon consideration of Eq. (A5), that the first-order constitutive equation is

$$\tau^{(1)}=2m|2e_{rz}^{(0)}|^{n-1}\left\{\mathbf{e}^{(1)}+[n-1]\frac{e_{rz}^{(1)}}{e_{rz}^{(0)}}\mathbf{e}^{(0)}\right\}. \tag{A9}$$

Upon consideration of the kinematic condition at the interface that

$$\overline{u_r^{(1)}}=\frac{\partial\zeta}{\partial t}\quad\text{at } r=\hat{r}, \tag{A10}$$

and the assumption of streamline parallel to the plates, it is clear from Eqs. (2a) and (A8b) that a solution is

$$u_r^{(1)}(r,\theta,z,t)=u(z)f_k'(t)\left[\frac{r}{\hat{r}}\right]^{-c(k)-1}\cos k\theta, \tag{A11a}$$

$$u_\theta^{(1)}(r,\theta,z,t)=\frac{c(k)}{k}u(z)f_k'(t)\left[\frac{r}{\hat{r}}\right]^{-c(k)-1}\sin k\theta, \tag{A11b}$$

where $f_k'(t)\equiv df_k/dt$. It remains to determine $u(z)$ which is a function purely of z and $c(k)$ which is a function of k. Then upon substitution of Eqs. (A11a) and (A11b) into Eq. (A9), the following expressions follow directly:

$$\tau_{rr}^{(1)}(r,\theta,z,t)=\tau_1(z)\frac{1}{r^n}f_k'(t)\left[\frac{r}{\hat{r}}\right]^{-c(k)-1}\cos k\theta, \tag{A12a}$$

$$\tau_{\theta\theta}^{(1)}(r,\theta,z,t)=\tau_2(z)\frac{1}{r^n}f_k'(t)\left[\frac{r}{\hat{r}}\right]^{-c(k)-1}\cos k\theta, \tag{A12b}$$

$$\tau_{r\theta}^{(1)}(r,\theta,z,t)=\tau_3(z)\frac{1}{r^n}f_k'(t)\left[\frac{r}{\hat{r}}\right]^{-c(k)-1}\sin k\theta, \tag{A12c}$$

$$\tau_{rz}^{(1)}(r,\theta,z,t)=\tau_4(z)\frac{1}{r^{n-1}}f_k'(t)\left[\frac{r}{\hat{r}}\right]^{-c(k)-1}\cos k\theta, \tag{A12d}$$

$$\tau_{\theta z}^{(1)}(r,\theta,z,t)=\tau_5(z)\frac{1}{r^{n-1}}f_k'(t)\left[\frac{r}{\hat{r}}\right]^{-c(k)-1}\sin k\theta, \tag{A12e}$$

where $\tau_1(z),\tau_2(z),\ldots,\tau_5(z)$ are functions purely of z and are yet to be determined. Then upon substitution of Eq. (A9) into Eq. (2b) and consideration of Eq. (A5), it can be easily shown that the momentum equation reduces to

$$\frac{\partial P^{(1)}}{\partial r}=\frac{\partial\tau_{rz}^{(1)}}{\partial z}, \tag{A13a}$$

$$\frac{1}{r}\frac{\partial P^{(1)}}{\partial\theta}=\frac{\partial\tau_{\theta z}^{(1)}}{\partial z}, \tag{A13b}$$

$$\frac{\partial P^{(1)}}{\partial z}=0. \tag{A13c}$$

From Eqs. (A12) and (A13) it is then clear that

$$P^{(1)}(r,\theta,z,t)=P_1\frac{g(t)}{r^{n-1}}\left[\frac{r}{\hat{r}}\right]^{-c(k)}\cos k\theta, \tag{A14}$$

where $g(t)$ and P_1 are yet to be determined. It must at this stage be noted that at the interface there are two contributing factors for the perturbed pressure: (i) the unperturbed pressure which gives rise to a term of order ζ, as is clear upon substitution of Eq. (A8a) into Eq. (A6a); and (ii) the actual perturbation to the pressure which is to be determined from the present perturbation analysis. These two factors must be taken into account in the evaluation of $g(t)$. Then upon consideration of Eqs. (A6a), (A12)–(A14), it can easily be shown that

$$g(t)=\frac{1}{P_1[1-c(k)-n]}\times\left\{\frac{nGf_k(t)}{\hat{r}}+\hat{r}\frac{d\tau_4^{(1)}(z)}{dz}f_k'(t)\right\}. \tag{A15}$$

However, from Eqs. (A12d) and (A13a) we immediately see that

$$\frac{d\tau_4^{(1)}(z)}{dz}=P_1[1-c(k)-n]\ . \tag{A16}$$

Therefore, upon substitution of Eq. (A16) into Eq. (A15) we obtain

$$\frac{1-c(k)-n}{r}P^{(1)}=\frac{mn}{r^{n-1}}\left\{-\frac{G}{m}\right\}^{(n-1)/n}\left[\frac{h}{2}-z\right]^{-1/n}\left[\frac{1-n}{n}\frac{\partial u_r^{(1)}}{\partial z}+\left[\frac{h}{2}-z\right]\frac{\partial^2 u_r^{(1)}}{\partial z^2}\right]\ , \tag{A18a}$$

$$-\frac{k}{r}P^{(1)}\tan k\theta=\frac{m}{r^{n-1}}\left\{-\frac{G}{m}\right\}^{(n-1)/n}\left[\frac{h}{2}-z\right]^{-1/n}\left[\frac{1-n}{n}\frac{\partial u_\theta^{(1)}}{\partial z}+\left[\frac{h}{2}-z\right]\frac{\partial^2 u_\theta^{(1)}}{\partial z^2}\right]\ . \tag{A18b}$$

Then from Eqs. (A12), (A14), and (A18), it can be easily shown in a similar manner to Wilson [18] that

$$u(z)=A_1\frac{n}{n+1}\left\{\left[\frac{h}{2}\right]^{(n+1)/n}-\left|z-\frac{h}{2}\right|^{(n+1)/n}\right\}\ , \tag{A19a}$$

with

$$c(k)=\frac{1-n+\sqrt{(1-n)^2+4k^2n}}{2}\ , \tag{A19b}$$

$$A_1=\frac{k^2}{c(k)m}P_1\left\{-\frac{G}{m}\right\}^{(1-n)/n}\ . \tag{A19c}$$

To obtain P_1, the kinematic condition Eq. (A10) is considered, from which we obtain

$$\overline{u(z)}=1\ . \tag{A20}$$

From Eqs. (A19) and (A20) we immediately obtain the solution

$$P_1=-\frac{c(k)}{k^2}\frac{G}{\hat{r}V}\ . \tag{A21}$$

Thus upon substitution of Eq. (A21) into Eq. (A17) and consideration of Eqs. (A7b) and (A19b) we find

$$g(t)=Vf_k(t)+\hat{r}f_k'(t)\ , \tag{A22}$$

which is very similar to the Newtonian result given by Bataille [21].

From Eqs. (A11), (A19a), and (A19c), all first-order stress components may be calculated directly using the first-order constitutive equation Eq. (A9), in a very straightforward manner. However, this is of no real value in the present analysis, since our primary concern is the examination of the behavior of the amplitude function $f_k(t)$. Hence, these stress components are omitted from the presentation.

$$g(t)=\frac{nGf_k(t)}{P_1[1-c(k)-n]\hat{r}}+\hat{r}f_k'(t)\ . \tag{A17}$$

Hence to complete the determination of $g(t)$, P_1 is clearly required, and we now evaluate it. Substituting Eq. (A9) into (A13), we find that

All that remains is the evaluation of the amplitude function $f_k(t)$. This is obtained upon consideration of the stress interface condition which is derived in an analogous manner to that in [18]:

$$\overline{P^{(1)}}+\frac{G\xi}{r^n}-\overline{\tau_{rr}^{(1)}}=\frac{\gamma(1-k^2)\xi}{r^2}\quad\text{at } r=\hat{r}\ , \tag{A23}$$

where γ is the interfacial surface tension. However, from Eqs. (A9), (A14), and (A21) it can be easily shown upon consideration of Eq. (A5) that

$$|\overline{P^{(1)}}|\gg|\overline{\tau_{rr}^{(1)}}|\ . \tag{A24}$$

It should also be noted that a similar result is obtained for $\overline{\tau_{\theta\theta}^{(1)}}$, although this term is clearly not present in Eq. (A23).

Therefore, using Eq. (A24), Eq. (A23) becomes

$$\overline{P^{(1)}}+\frac{G\xi}{r^n}=\frac{\gamma(1-k^2)\xi}{r^2}\quad\text{at } r=\hat{r}\ . \tag{A25}$$

Following substitution of Eqs. (A8b), (A14), and (A21) into Eq. (A25), the governing equation for $f_k(t)$ directly follows and is

$$\frac{1}{f_k}\frac{df_k}{dt}=\frac{G}{P_1\hat{r}^2}\left\{\frac{c(k)}{k^2}-1\right\}-\frac{\gamma(k^2-1)\hat{r}^{n-4}}{P_1}\ , \tag{A26}$$

whose solution is

$$f_k(t)=At^{1/2\{[k^2/c(k)]-1\}}\times\exp\left\{\frac{2\gamma(k^2-1)}{(2-n)b^{4-n}P_1t^{(2-n)/2}}\right\}\ , \tag{A27}$$

where A is an arbitrary constant. As the amplitude function is determined, the analysis is complete.

[1] A. L. Robinson, Science **228**, 1077 (1985).
[2] L. M. Sander, Nature **314**, 405 (1985).
[3] G. M. Homsy, Annu. Rev. Fluid Mech. **19**, 271 (1987).
[4] A. A. Sonin, Riv. Nuovo Cimento **14**, 1 (1991).
[5] J. Nittmann, G. Daccord, and H. E. Stanley, Nature **314**, 141 (1985).
[6] J. Nittmann, G. Daccord, and H. E. Stanley, in *Fractals in Physics,* edited by L. Pietronero and E. Tosatti (Elsevier,

Amsterdam, 1986), p. 193.
[7] J. Nittmann, Physica A **140**, 124 (1986).
[8] G. Daccord and J. Nittmann, Phys. Rev. Lett. **56**, 336 (1986).
[9] H. Van Damme, F. Obrecht, P. Levitz, L. Gatineau, and C. Laroche, Nature **320**, 731 (1986).
[10] H. Van Damme, C. Laroche, and L. Gatineau, Rev. Phys. Appl. **22**, 241 (1987).
[11] E. Allen and D. V. Boger, in *Proceedings of the Xth International Congress on Rheology, Sydney, 1988,* edited by P. H. T. Uhlherr (Australian Society of Rheology, Sydney, 1988), Vol. 1, p. 146.
[12] H. Van Damme, E. Alsac, C. Laroche, and L. Gatineau, Europhys. Lett. **5**, 25 (1988).
[13] H. Van Damme, E. Alsac, and C. Laroche, C. R. Acad. Sci. Paris. II **309**, 11 (1989).
[14] T. Nagatani, Phys. Rev. A **41**, 994 (1990).
[15] E. Lemaire, P. Levitz, and H. Van Damme, C. R. Acad. Sci. Paris II **311**, 1467 (1990).
[16] J. Nittmann and H. E. Stanley, Nature **321**, 663 (1986).
[17] H. Pascal, J. Colloid Interface Sci. **123**, 14 (1988).
[18] S. D. R. Wilson, J. Fluid Mech. **220**, 413 (1990).
[19] A. L. Robinson, Science **228**, 834 (1985).
[20] P. G. Saffman, J. Fluid Mech. **173**, 73 (1986).
[21] J. Bataille, Rev. Inst. Fr. Pet. **23**, 1349 (1968).
[22] S. D. R. Wilson, J. Colloid Interface Sci. **51**, 532 (1975).
[23] L. Paterson, J. Fluid Mech. **113**, 513 (1981).
[24] L. Paterson, Phys. Fluids **28**, 26 (1985).
[25] E. Ben-Jacob, R. Godbey, N. D. Goldenfeld, J. Koplik, H. Levine, T. Mueller, and L. M. Sander, Phys. Rev. Lett. **55**, 1315 (1985).
[26] C. Couder, O. Cardoso, D. Dupuy, P. Tavernier, and W. Thom, Europhys. Lett. **2**, 437 (1986).
[27] S. D. Howison, J. Fluid Mech. **167**, 439 (1986).
[28] S. N. Rauseo, P. D. Barnes, Jr., and J. V. Maher, Phys. Rev. A **35**, 1245 (1987).
[29] J. D. Chen, Exp. Fluids **5**, 363 (1987).
[30] J. D. Chen, J. Fluid Mech. **201**, 223 (1989).
[31] S. K. Sarkar and D. Jasnow, Phys. Rev. A **39**, 5299 (1989).
[32] S. E. May and J. V. Maher, Phys. Rev. A **40**, 1723 (1989).
[33] S. K. Sarkar, Phys. Rev. Lett. **65**, 2680 (1990).
[34] P. G. Saffman and G. I. Taylor, Proc. R. Soc. London Ser. A **245**, 312 (1958).
[35] J. V. Maher, Phys. Rev. Lett. **54**, 1498 (1985).
[36] D. A. Kessler and H. Levine, Phys. Fluids **30**, 1246 (1987).
[37] A. R. Kopf-Sill and G. M. Homsy, Phys. Fluids. **31**, 242 (1988).
[38] P. G. Saffman, IMA J. Appl. Math. **46**, 137 (1991).
[39] D. Jasnow and C. Yeung, Phys. Rev. E **47**, 1087 (1993).
[40] R. Binnington (private communication).
[41] E. Weisser (private communication).
[42] H. Van Damme, C. Laroche, L. Gatineau, and P. Levitz, J. Phys. (Paris) **48**, 1121 (1987).
[43] E. Lemaire and H. Van Damme, C. R. Acad. Sci. Paris. II **309**, 859 (1989).
[44] E. Lemaire, P. Levitz, G. Daccord, and H. Van Damme, Phys. Rev. Lett. **67**, 2009 (1991).
[45] K. S. Lee and E. L. Claridge, Soc. Pet. Eng. J. **8**, 52 (1968).

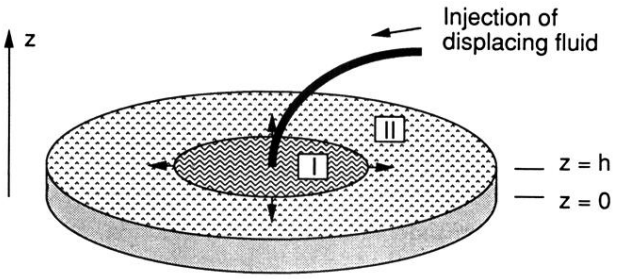

FIG. 1. Schematic illustration of the radial Hele-Shaw cell, showing injection of displacing fluid into region I and the consequent displacement of the fluid in region II. Arrows around the interface between regions I and II indicate the direction of flow. The origin of the cylindrical coordinate system is taken at the center of the bottom plate, with the z direction as indicated.